Evaluation of early-stage dissolution of spent NdFeB permanent magnets in organic acids by in-situ quantitative reflected light microscopy

Pucci Couto, Camila; Mopon, Marlon; Venkatesan, Prakash; Ustarroz, Jon; Yang, Yongxiang; Garcia, Santiago J.; Abrahami, Shoshan T.

DOI
10.1016/j.jmrt.2025.11.006

Publication date
2025

Document Version
Final published version

Published in
Journal of Materials Research and Technology

Journal of Materials Research and Technology 39 (2025) 6981–6993

Contents lists available at ScienceDirect

Journal of Materials Research and Technology

journal homepage: www.elsevier.com/locate/jmrt

Evaluation of early-stage dissolution of spent NdFeB permanent magnets in organic acids by *in-situ* quantitative reflected light microscopy

Camila Pucci Couto [a], Marlon Mopon [b,c], Prakash Venkatesan [d], Jon Ustarroz [e,f], Yongxiang Yang [a], Santiago J. Garcia [b], Shoshan T. Abrahami [a,*]

[a] Department of Materials Science and Engineering, Faculty of Mechanical Engineering, Delft University of Technology, Mekelweg 2, 2628 CD, Delft, the Netherlands
[b] Aerospace Structures and Materials Department, Faculty of Aerospace Engineering, Delft University of Technology, Kluyverweg 1, 2629 HS, Delft, the Netherlands
[c] Department of Chemical Engineering, University of the Philippines, Diliman, Quezon City, Philippines
[d] Department of Materials Engineering, Synthesis and Recycling (4MAT), Université Libre de Bruxelles, Avenue FD Roosevelt 50, CP165/63, 1050, Brussels, Belgium
[e] Chemistry of Surfaces, Interfaces and Nanomaterials (ChemSIN), Université Libre de Bruxelles, Campus de La Plaine, Boulevard Du Triomphe 2, CP 255, 1050, Brussels, Belgium
[f] Research Group Electrochemical and Surface Engineering (SURF), Vrije Universiteit Brussel, Pleinlaan 2, 1050, Brussels, Belgium

ARTICLE INFO

Keywords:
Critical-raw materials
NdFeB
Rare-earth elements
Dissolution
Organic acids

ABSTRACT

A hyphenated optical-electrochemical set-up was used to investigate the early-stage dissolution mechanism of NdFeB permanent magnets immersed in acetic, citric, and formic acids at concentrations of 0.01 and 0.1 M. This approach enabled a direct correlation between quantifiable surface changes and dissolution behaviour under open-circuit potential (OCP) conditions. Despite minimal OCP variation (180 mV) across all conditions and rapid stabilisation within approximately 300 s, significant optically-detectable surface changes continued throughout the measurement period (1 h). This emphasises that surface dissolution kinetics, rather than thermodynamics, predominantly control the early-stage dissolution of NdFeB. Kinetic parameters obtained by fitting mean activity-level curves with a sigmoidal model revealed that higher acid concentrations result in shorter induction periods and faster surface activation. *In-situ* optical analysis indicated a consistent dissolution mechanism characterised initially by localised activation, followed by the progressive expansion of active sites across the surface. Post-immersion analysis confirmed preferential dissolution of rare-earth-rich phases at grain boundaries and triple points, alongside intragranular dissolution observed in 0.01 M citric acid. Among the tested conditions, dilute citric acid (0.01 M) emerges as particularly suitable medium for practical control, as its relatively long induction period (~1378 s) allows monitoring and controlling local dissolution before rapid surface activation begins. The combined optical-electrochemical approach also revealed that, while rare-earth-rich sites are preferentially activated, early signs of matrix activation are detectable, underscoring the value of *in-situ* optical analysis for advancing process control in NdFeB recycling.

1. Introduction

One of the key highlights of the 2023 United Nations Climate Change Conference (COP) was the reinforced commitment to reduce global greenhouse gas emissions by 50 %, aiming to achieve the goal of net-zero emissions by 2050 [1]. Such a goal can only be reached by promoting an effective energy transition from fossil fuels to renewable sources [2]. Yet, the energy transition relies on significant growth in applications containing critical raw materials (CRMs). A prominent example is rare-earth elements (REEs), which are needed to produce strong permanent magnets (PMs) for wind turbines, hybrid and electric vehicles, e-bikes, e-scooters, and many other high-tech applications which drives our modern life, including laptops and smartphones [3–9].

The EU has classified REEs among the most critical materials due to their economic importance and supply risk [10]. Currently, the REEs value chain, from mining to magnet production, remains highly centralised [10,11]. Considering the importance of CRMs, the EU has introduced the "Critical Raw Materials Act" (CRMA) which outlines strategies to ensure continuous supply of CRMs in Europe [12,13]. One of these strategies focuses on recycling end-of-life (EoL) products containing CRMs. As a benchmark, the EU has set a goal to recycle at least 25 % of its annual consumption of CRMs by 2030 [13]. According to the

* Corresponding author.
E-mail address: S.T.Abrahami@tudelft.nl (S.T. Abrahami).

https://doi.org/10.1016/j.jmrt.2025.11.006
Received 25 August 2025; Received in revised form 29 October 2025; Accepted 3 November 2025
Available online 7 November 2025

CRMs report published in 2023, the recycling rate of REEs in Europe is only 1 % [10]. Therefore, significant efforts are needed to optimise recycling processes, making them more efficient and sustainable [3,7,14–20].

Hydrometallurgical processes for recovering REEs from NdFeB PMs have been extensively studied [5,6,8,21–23]. These processes are particularly effective for targeting heterogeneous scrap, such as shredded electronic waste [22,24]. In hydrometallurgy, leaching is the initial operation aimed at dissolving target materials. This step plays a critical role in subsequent stages, including extraction, separation, and recovery [8]. For example, in NdFeB PMs, leaching in acidic media typically dissolves the complete magnet [8]. Due to this lack of selectivity, multiple separation steps are often required to isolate the REEs in the subsequent solution purification steps. In some cases, selectivity is achieved by roasting the scrap before leaching to promote the oxidation of metals, thereby enhancing the leaching selectivity of REEs over iron [25–27]. However, this extra step, considered part of scrap pre-treatment, leads to higher energy consumption and additional emissions. Conversely, electrochemical methods can target specific elements, while offering benefits such as minimal energy and chemicals consumption and enhanced reaction kinetics [14,15,17,28]. Various approaches have been proposed for electrochemical leaching (electroleaching) using both organic and inorganic acids [14–17,28]. These studies highlight the potential of leaching under electrochemical conditions, achieving high extraction efficiency for Nd and Fe at low acid concentrations.

Optimising either a chemical or electrochemical leaching process for selective dissolution of the REEs over other elements in the NdFeB alloy, requires an understanding of the dissolution kinetics and mechanism of the different phases within the NdFeB microstructure. According to the literature, the microstructure of NdFeB consists of a $Nd_2Fe_{14}B$ ferromagnetic matrix, surrounded by a Nd-rich phase (Nd_4Fe) that forms triple points, and a paramagnetic boride phase ($NdFe_4B_4$) located at the grain boundaries [29–35]. Moreover, depending on the application of the NdFeB PMs, other REEs are often added, including Pr, Dy, Tb and Ce [3,5,8,9,23,36,37]. Therefore, the Nd-rich phase is often referred to as RE-rich phase.

Previous studies have shown that the dissolution of bulk NdFeB PMs in neutral and acidic solutions starts in the grain boundaries which are enriched with REEs, followed by the dissolution of the RE-rich phase, and lately the matrix. NdFeB matrix behaves as the cathode and RE-rich phases as the anode; this imbalance, with a larger cathodic surface area, leads to degradation and eventual disintegration of the $Nd_2Fe_{14}B$ grains [29,32,38–40]. In alkaline media, and in phosphoric acid or oxalic acid, NdFeB tends to form a protective oxide layer, with its stability depending on the specific nature of the electrolyte [33,40,41].

This high-dissolution susceptibility of the RE-rich phase is attributed to its high reactivity, as indicated by the low standard oxidation electrode potential of REEs (approximately −2.2 to −2.5 V) [32]. Even though the dissolution mechanism of NdFeB PMs has been extensively investigated [30,32,33,39,42], most works have relied on electrochemical measurements combined with post-microstructural analysis. This approach unfortunately leads to the loss of information on early-stage processes and local dissolution phenomena. Capturing the surface activity occurring during early-stage immersion could provide valuable insights into the selective dissolution of REEs, particularly in assessing their preferential leaching over other alloying elements.

A comparable challenge is common in corrosion research, where microstructural changes are often analysed after electrochemical testing (postmortem) or identified once the corrosion process is significantly advanced, hence losing significant information. To address this challenge, hyphenated methodologies combining electrochemistry and high-resolution optics have been recently proposed [43–50]. For instance, optical-electrochemical setups which enable the simultaneous monitoring of target surfaces using electrochemical techniques (e.g. impedance (EIS)) and optics (time resolved micrographs), turned into quantifiable information after data imaging processing protocols, are implemented [43–47]. The effectiveness of this approach is attributed to its simple and cost-effective hardware combined with image processing protocols allowing to quantify information with high spatial (pixel resolution ~1 μm^2) and time resolution (1 s), which can be directly correlated to electrochemical signals. For example, this approach has been successfully applied to monitor surface changes during impedance measurements in the study of aluminium alloy corrosion inhibition [44] and to investigate intermetallic dealloying and trenching in aluminium alloys [46]. Naturally, these setups continue to evolve, aiming to improve resolution and *in-situ* correlation of localised phenomena. By coupling reflective microscopy with electrochemical measurements, researches have successfully monitored different stages of iron oxidation [51] and the rapid selective deposition and growth of cerium oxides as function of the inter metallic composition on AA2024-T3 alloys [47]. Moreover, advancements in imaging techniques have enabled the detection of chemical crosstalk between particles in aluminium alloys, utilising not only reflective microscopy but also fluorescence microscopy [52].

The previous examples highlight the numerous possibilities for cost-effective *in-situ* methods in correlating electrochemical signals to surface phenomena. Hence, it offers a new way to study fast-changing systems such as magnet alloy dissolution. This study investigates, for the first time, the early-stage dissolution of spent NdFeB permanent magnets in dilute acetic, citric, and formic acids using an in-situ optical–electrochemical set-up. The method enables simultaneous OCP monitoring and time-resolved optical imaging, from which we derive quantitative surface-activity metrics. Our objective is to correlate OCP with optical activity maps to track the onset and propagation of RE-preferential dissolution. In this context, OCP monitoring can be correlated with standard chemical leaching in hydrometallurgical processes. Organic acids were selected for their reported high leaching efficiencies towards REEs [17,19,36,37], as well as for being biodegradable and easier to handle compared to inorganic acids [20,53,54].

2. Experimental

2.1. Samples

Samples of NdFeB PMs were obtained by manual disassembling of spent hard-disc drives and E-scooter rotor. After removing the magnets, they were demagnetised in a furnace at 400 °C for 30 min and air-cooled to room temperature. The demagnetised samples were cut into pieces of 5 × 5 mm and then mounted in hot resin (Bakelite). Finally, the samples were ground with SiC papers (#80 - #2000) and then polished with diamond suspension (3 - 1 μm).

2.2. Optical-electrochemical set-up

A schematic representation of the setup used in this work, adapted from [44,45], is shown in Fig. 1. The embedded NdFeB samples were placed in the optical-electrochemical set-up comprised of an electrochemical cell (redox.me Raman electrochemical flow cell) and a reflected light microscope (Dinolite AM7515MT4A, ≈10-pixel μm^{-2}). The samples served as the working electrode and Ag/AgCl (3 M KCl) electrode integrated into the electrochemical cell was used as the reference electrode. Electrochemical measurements were facilitated with an Ivium CompactStat.h potentiostat.

Image capture and potential measurements were initiated prior to the introduction of the electrolyte into the cell to enable collection of data from the very start of exposure. Around 5 mL of the electrolyte was injected with a syringe to fully expose the surface of the embedded sample. Open-circuit potential (OCP) of NdFeB samples was measured for 1 h in acetic and citric acids at concentrations of 0.01 M and 0.1 M. The OCP in 0.01 M formic acid was also measured over 1 h, whereas in 0.1 M formic acid the measurement was stopped after 20 min due to

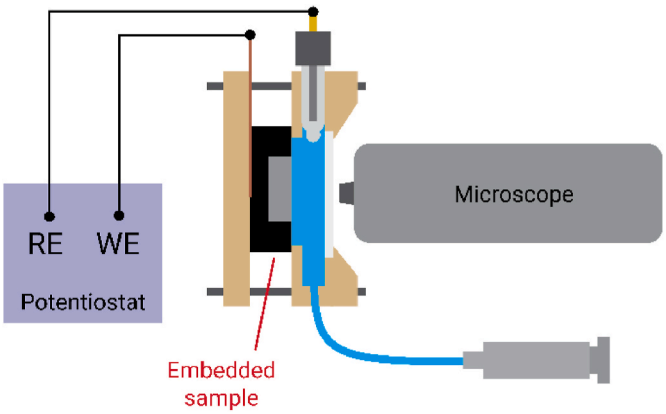

Fig. 1. Schematic view of the optical-electrochemical set-up, highlighting the vertical position of both sample and camera. Adapted from [46].

intense bubble formation. The reagents used were acetic acid (analytical reagent grade, 99–100 %, Boom), citric acid (extra pure crystals, Boom), and formic acid (ACS reagent, ≥96 %, Sigma-Aldrich), and solutions were prepared with Milli-Q water (18.2 MΩ cm). All measurements were carried out at room temperature, while simultaneously recording optical images under axial lighting (i.e., brightfield mode). While the whole sample was exposed to the electrolyte, the area under direct optical observation is only a fraction (≈0.95 × 0.71 mm^2) of the total area. Measurements for each condition were performed in duplicate to evaluate reproducibility.

2.2.1. Image analyses

The acquired images were processed using an image analysis protocol discussed in detail elsewhere [46,47]. While those protocols include the use of an intensity threshold, in this study surface changes were quantified solely through direct subtraction of pre-processed images (converted to 8-bit grayscale and recursively aligned), without applying any threshold. For the NdFeB samples, surface changes were visually identifiable as *pixel darkening* in raw images, which was then quantitatively assessed using image subtraction. The subtraction is performed against a reference image, typically the image at $t = 0$ s of immersion in the electrolyte (i.e., image at $t = 0$ s - image at a given time *(x)* s) unless otherwise stated. The output of the subtraction is the 8-bit *activity map* at *x* seconds. The value of each pixel in the map indicates how much change occurred (i.e., *activity level*) with respect to the reference image. The activity level ranges from 0 to 255. It is noted that an activity level of 255 is only possible when the initial surface completely reflects light. Pixels that did not register any additional darkening with respect to the reference image have an activity level of 0. Meanwhile, those that show more substantial darkening exhibit much higher values. For easier visualisation of the activity levels, the activity maps were coloured in ImageJ. In the coloured images, pixels with higher activity levels appear as brighter/warmer pixels.

The time-dependence of the changes depicted in the activity maps was determined by measuring the mean activity level at a given time of all the pixels in the field of view of the microscope. In some cases, the mean activity level curve may show discontinuities due to brightness changes during data acquisition. This can register in the curves as step discontinuity. If this occurs, the discontinuity is corrected numerically by applying an offset equivalent to the magnitude of the step.

To obtain the dissolution kinetics and overall surface degradation kinetics, the mean activity level curves were analysed using different curve-fitting models, including linear, quadratic, exponential, and sigmoidal, in Python (see Supplementary Information (SI 1.1)). The best-fitting model was selected based the coefficient of determination (R^2) and residual analysis.

2.3. Pre exposure and post exposure sample characterisation

Samples from different end-of-life (EoL) products were characterised prior to immersion experiments to determine their composition and the distribution of RE-rich phases. All samples were characterised after the tests using scanning electron microscopy (SEM), Jeol JSM-IT100. The semi-quantitative elemental composition was determined by energy dispersive X-ray spectroscopy (EDS). SEM images were acquired in both secondary electron (SE) and backscattering electron (BSE) modes. The microscope was set to operate with an acceleration voltage of 20 kV, probe current of 60 pA, and a working distance between 10 and 12 mm.

3. Results and discussion

3.1. Characterisation of the initial condition of a spent NdFeB PM

Fig. 2 shows a representative initial condition of the NdFeB microstructure, before immersion. It is consistent with the characterisation of Zakotnik et al., [34]; the ferromagnetic matrix is characterised by a dark grey colour, while grain boundaries consisting of the paramagnetic phase, and the RE-rich phases, also known as triple points [32,35], are represented by a white (1) and light grey (2) contrast. The light grey contrast (2) is related to the higher oxygen and lower REEs content than the brightest phase (1). Furthermore, grains can be recognised in the SEM image, with an average grain size of about 5.8 μm, as determined by the method Heyn Linear Intercept Procedure in accordance with ASTM E112-24 [55]. Additional measurements using ImageJ, across five micrographs of different samples, revealed that the RE-rich phases (triple points and grain boundaries) represent about 8 % (±1.5 %) of the surface area. Another important parameter is the thickness of the grain boundaries, which has been reported in the nanometre range [56–58].

As mentioned previously, samples were obtained from both HDDs and E-scooters, and Fig. 2presents a sample from an E-scooter. Nevertheless, the microstructural morphology does not differ significantly between the two sources, as shown in our previous study [3]. There are, however, slight variations in composition; but overall, the total REE content is nearly the same in both applications [3].

3.2. Correlation between the open-circuit potential and the mean activity level

Fig. 3 shows representative reflected light microscopy images of the NdFeB sample acquired before, during, and after immersion in 0.01 M citric acid. Prior to immersion (Fig. 3 (a)), the surface consists of a

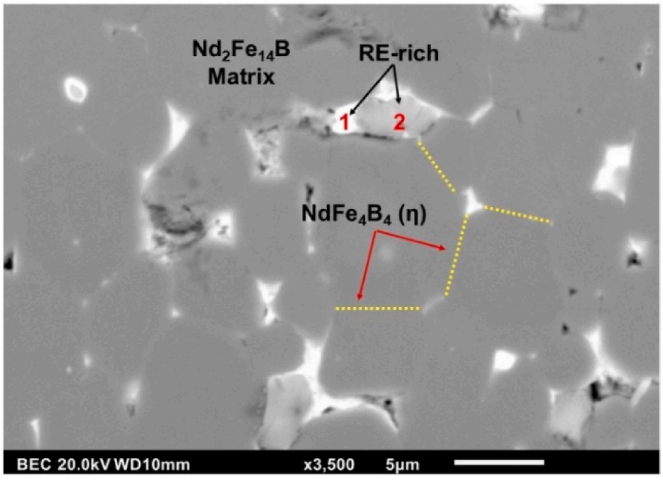

Fig. 2. SEM image of the initial condition of NdFeB microstructure, highlighting the $Nd_2Fe_{14}B$ ferromagnetic matrix, the RE-rich phases and the $NdFe_4B_4$ paramagnetic phase at the grain boundaries.

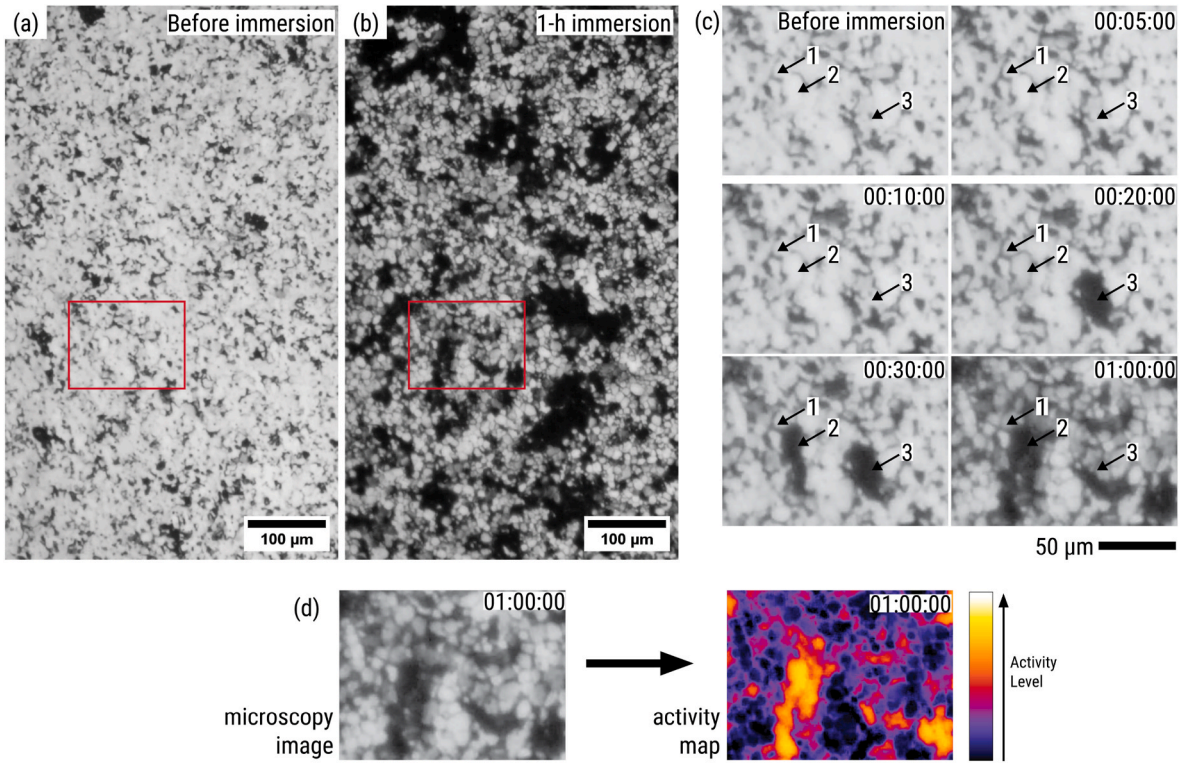

Fig. 3. Reflected light microscopy images of the sample (a) before immersion, (b) after 1 h of exposure to 0.01 M citric acid, and (c) at different times during immersion for the region indicated by the red rectangle. A microscopy image and its corresponding activity map is shown in (d).

continuous grey matrix interspersed with darker domains. The grey regions correspond to the $Nd_2Fe_{14}B$ matrix, while the darker domains are likely associated with RE-rich phases or other surface irregularities previously observed in the pre-immersion SEM image (Fig. 2). Upon immersion in the acidic electrolyte (Fig. 3(b)), the surface undergoes pronounced changes, including increased contrast along grain boundaries, progressive darkening of grains, and the formation of larger dark patches. A closer inspection of a selected area (Fig. 3 (c)) reveals that these changes can be categorised into three types: (1) darkening of grain boundaries, (2) irreversible darkening of grain domains, and (3) reversible darkening of grain domains. The reversible darkening behaviour, as observed at point 3, between 30 min and 1 h of immersion, corresponds to transient contrast changes where the initially darkened regions later fade; but, subsequently darken again with continued exposure. The darkening of grain boundaries initially displays reversible behaviour, with the regions darkening and then partially brightening between 5 and 20 min of immersion, after which the contrast gradually becomes permanently dark at longer exposure times.

The presence of darkened domains even before immersion complicates the direct interpretation of surface changes from the microscopy images. To address this, the image subtraction protocol described in the methodology section was applied to generate the activity maps shown in Fig. 3 (d). These maps provide a semi-quantitative means of identifying where changes occur and estimating their extent. By calculating the average activity from the maps, the time dependence of the overall surface evolution can be evaluated and correlated with the concurrent OCP measurements. Fig. 4 presents the OCP and mean activity curves derived from the activity maps for all evaluated conditions, with the selected curves representing the general trends observed across all measurements.

3.2.1. *Open-circuit potential evolution*

Based on Fig. 4, the OCP evolution of NdFeB in different organic acids exhibits a similar trend; an initial potential drop of 0.3–0.5 V occurs within the first 50–200 s, followed by stabilisation. The initial potential drop, observed in all conditions, is characteristic of breakdown of the oxide film naturally formed on the sample surface of active systems such as the NdFeB alloy [59]. Although the characterisation of an oxide layer is beyond the scope of this work, it is well known that NdFeB is easily oxidised in air, justifying the need for a protective coating during its use to avoid loss of magnetic properties due to oxidation [60].

After the initial drop, OCP stabilises at negative potentials, indicating steady-state dissolution at all conditions. When comparing the final OCP values, little difference is observed among the different organic acids, with a maximum variance of only 180 mV, based on the average measured during the last minute of measurement. The highest value of −520 mV was observed in 0.1 M citric acid, and the lowest, −700 mV, in 0.01 M formic acid. These values can be related to the acids' strengths, as reflected by their similar pKa values: acetic acid has a pKa of 4.76; citric acid, with three carboxylic groups, has pKa values of 3.13, 4.76, and 6.40; and formic acid has a pKa of 3.8 [19,20]. Theoretically, a lower pKa results in a lower pH solution, shifting the OCP towards more positive values [61], which agrees with the behaviour observed for citric acid, but not for formic acid.

This contradiction indicates that the proton availability from organic acids alone does not exclusively govern the dissolution of NdFeB magnets [19]. Gergoric et al. [20] have demonstrated that the dissolution mechanism of NdFeB in organic acids initially involves displacement of the rare-earth ions from the alloy structure by hydronium ions, followed by the formation of metal-organic complexes. Importantly, the stability of these complexes significantly influences the dissolution efficiency. Citric and acetic acids are known to form soluble complexes with REEs, whereas formic acid form insoluble complexes [19].

Regarding acid concentration, no straightforward relationship between higher concentration and lower OCP was observed. In other words, increasing the acid concentration did not consistently result in lower OCP values. Notably, in 0.1 M formic acid, intense bubble formation hindered continuous monitoring beyond 1800 s. The bubbles

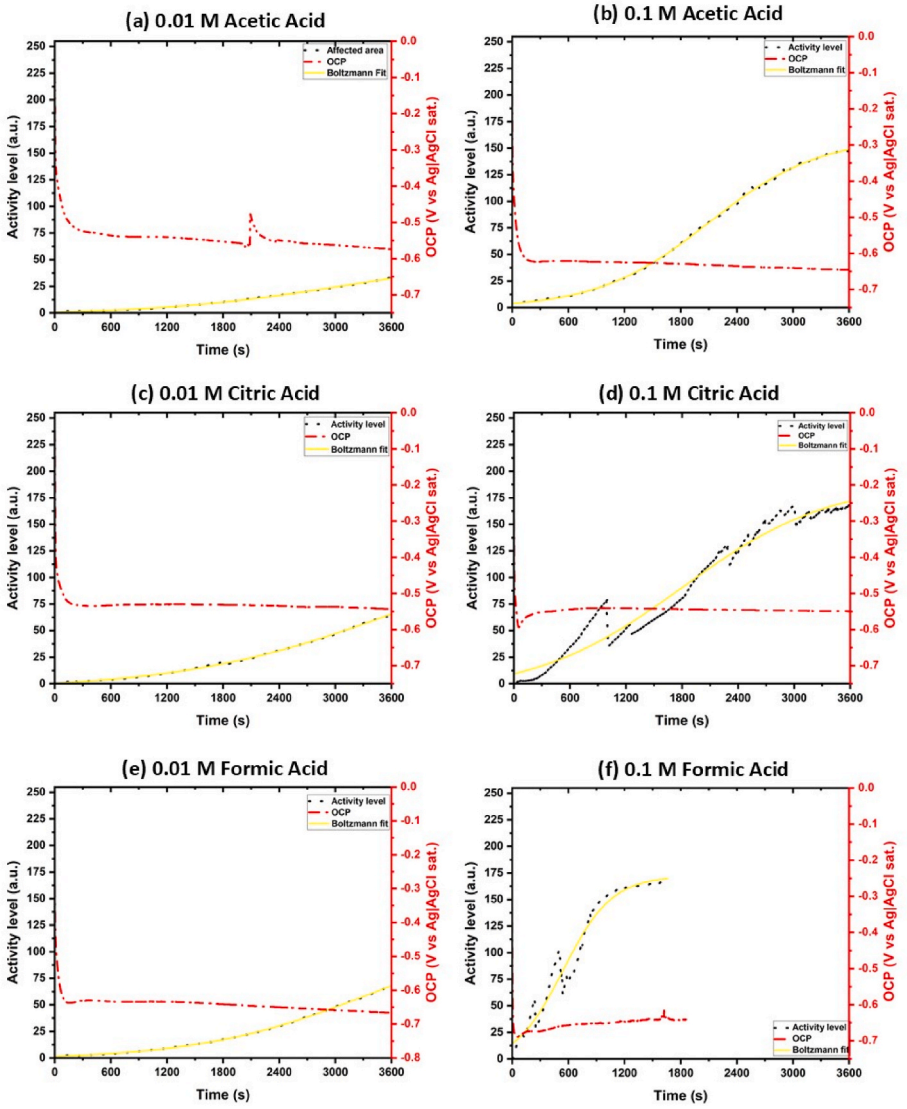

Fig. 4. Evolution of the open-circuit potential (OCP, dashed-dot line) and activity level (dotted line) of NdFeB, together with the sigmoidal fit (solid line), for 3600 s in (a) 0.01 M acetic acid, (b) 0.1 M acetic acid, (c) 0.01 M citric acid, (d) 0.1 M citric acid, (e) 0.01 M formic acid, and for 1800 s in (f) 0.1 M formic acid.

have been attributed to H_2 gas evolution, a reaction product between the acid and the NdFeB alloy [18,19,40].

Although the OCP stabilises rapidly for all conditions (within ≈300 s), the mean activity level curves in Fig. 4 indicate that surface changes continue to progress throughout the entire measurement period. According to El-Moneim et al. [30], the dissolution mechanism of NdFeB in N_2-purged 0.1 M H_2SO_4 under open-circuit conditions occurs in three stages: the first stage (1–3 min) involves preferential attack at the grain boundaries, followed by dissolution of the more anodic RE-rich phases, and finally, matrix dissolution, which begins approximately 6–7 min after immersion. It is important to note, however, that the authors did not present OCP curves; their proposed mechanism was based on elemental dissolution rate measurements (mass loss combined with ICP-OES measurements). Similarly, Koshsima et al. [36] concluded that selective dissolution of RE-rich phases from powdered NdFeB can be achieved within 15 min in 1 M citric acid. Their *ex-situ* analyses indicated selective removal of REEs at grain boundaries and triple points, while the matrix was largely preserved.

3.2.2. *Surface changes captured by activity maps*

Fig. 4 also shows the evolution of surface changes in NdFeB samples during immersion in organic acids, evaluated by the mean activity level curves. It is worth noting that some curves exhibit spikes, particularly in Fig. 4 (d) and more prominently in Fig. 4 (f), for 0.1 M citric and formic acids, respectively. These spikes resulted from the rapid formation and detachment of H_2 bubbles from the surface. The bubbles scatter light effectively resulting to sudden increase in the mean activity-level. However, once the bubbles detach, the area covered by the bubble reflects light again (i.e., appears less dark) which leads to the observed drop in the mean activity level. As this process was too intense in the 0.1 M formic acid, the measurement was interrupted once the optical changes observed plateaued to avoid issues that might arise from pressure accumulation in the electrochemical cell.

To quantitatively describe the kinetics of these surface changes, the mean activity level curves were fitted using a sigmoidal model, which captures three main stages: an initial induction period with minimal surface changes, a phase of rapid activity growth, and a final plateau [62]. The fitted curves and equations for each condition are provided in the SI 1.2. From these fits, three key parameters were extracted and reported in Table 1: the induction period, the inflection point, and the rate of change. The induction period reflects the time before rapid dissolution begins; the inflection point marks the time of maximum slope, i.e., the fastest rate of surface change; and the rate of change quantifies how sharply this transition occurs. The induction period was

Table 1
Induction time, inflection point and rate of change parameters extracted from sigmoidal equations fitted to the data in Fig. 4, which describes the affected area evolution under different conditions.

	Acetic Acid		Citric Acid		Formic Acid	
	0.01 M	0.1 M	0.01 M	0.1 M	0.01 M	0.1 M
Induction period (s)	1110	913	1378	209	1543	20
Inflection point (s)	3127	2103	3731	1803	3366	542
Rate of change	1008	595	1176	797	912	261

determined by the geometric method (see SI 2).

As seen in Table 1, high acid concentrations resulted in much shorter induction periods and earlier inflection points. For example, 0.1 M formic acid exhibited an almost negligible induction period (20 s) and the earliest inflection point (542 s), indicating an intense and abrupt onset of surface activity. In contrast, lower acid concentrations resulted in longer induction periods and delayed inflection points, e.g., 1110 s and 3127 s, respectively, for 0.01 M acetic acid consistent with a slower initiation of dissolution. Interestingly, these longer induction periods occurred even though the OCP had already stabilised. This suggests that certain surface phenomena causing minimal optical response, i.e., low-level pixel changes, may still occur during this time. One possibility is the dissolution of a native oxide layer upon initial immersion, which would account for the initial OCP drop, while causing only subtle surface changes not yet distinguishable in the averaged optical signal.

The inflection point and rate of change are inherently linked kinetic parameters that together describe the dynamics of surface activation. The inflection point marks when the surface activity increases most rapidly, while the rate of change defines the speed of this transition. In more diluted solutions, the transition from induction to (an eventual) plateau is broader and more gradual, which results in a higher calculated rate of change, even though the actual process is slower and more extended, as seen for 0.01 M citric acid. Conversely, the low rate of change observed for 0.1 M formic acid (261) reflects an extremely rapid, localised transformation, as seen from its nearly absent induction period. As these parameters were derived by fitting a sigmoidal model to the mean activity-level curves, the conditions with extended or incomplete transitions within the measurement period (3600 s) resulted in calculated inflection points beyond the actual monitoring duration. This was observed in all diluted conditions. It is important to note that spikes caused by bubbling, mainly in the 0.1 M citric and formic acid conditions, can affect the reliability of the fitted parameters. Thus, kinetic

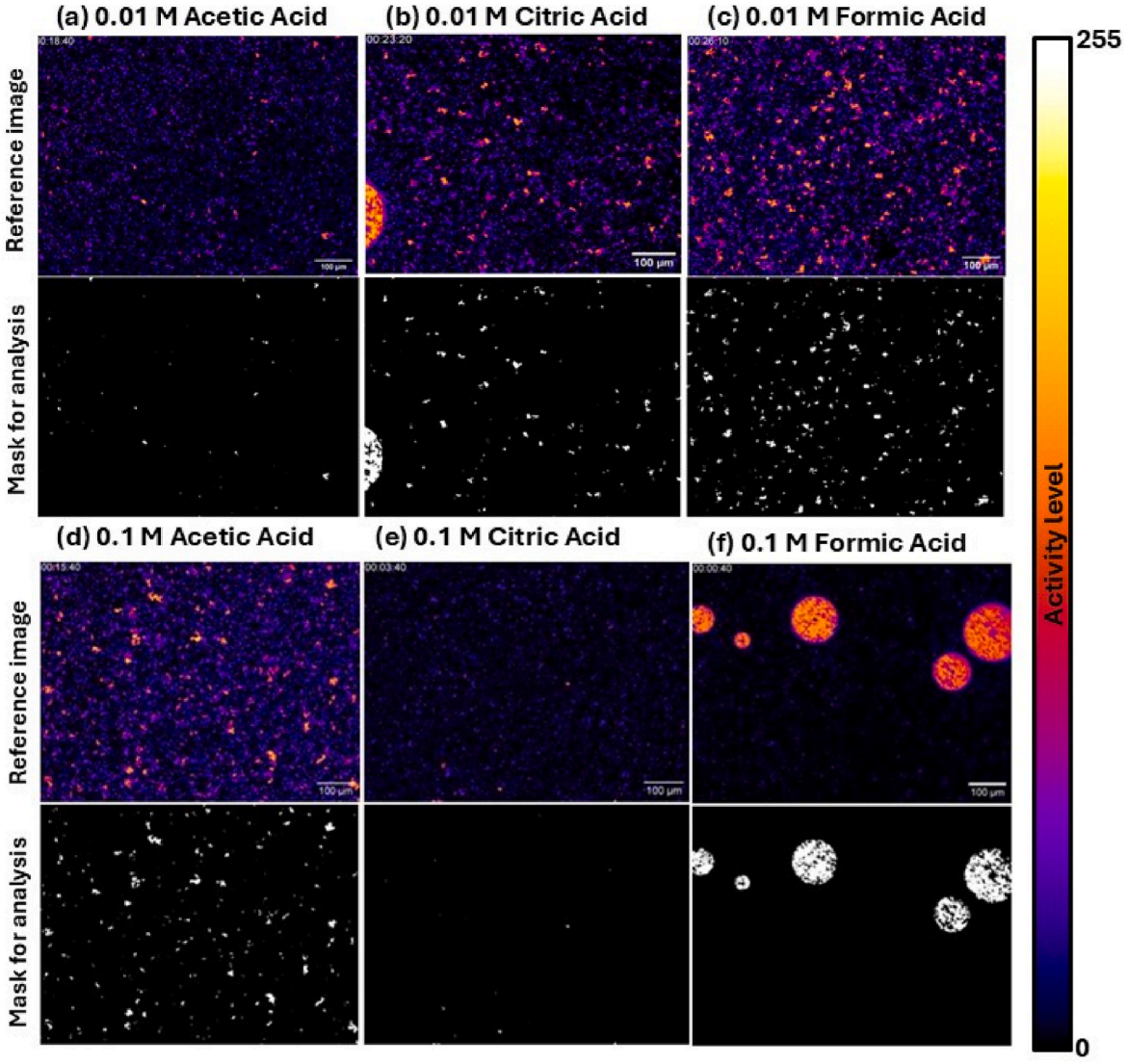

Fig. 5. Local activity maps of the NdFeB surface at the end of the induction period for each condition, with their corresponding mask images used for quantification of high-activity regions (red/orange) contrast: (a) 0.01 M acetic acid, (b) 0.01 M citric acid, (c) 0.01 M formic acid, (d) 0.1 M acetic acid, (e) 0.1 M citric acid, and (f) 0.1 M formic acid.

values from these conditions should be interpreted with caution. Nonetheless, the general trend remains clear: higher acid concentrations accelerate both the onset and the rate of surface changes. Since OCP did not vary significantly among the conditions, these results highlight that surface dissolution kinetics, rather than thermodynamic driving force, predominantly control the early-stage dissolution of NdFeB under the tested conditions. This also helps explain why surface changes in 0.1 M formic acid are so pronounced, resulting in high activity levels compared to the other conditions, particularly in the initial stage, as seen in Fig. 4.

3.2.3. Time-images correlation

A major advantage of the optical-electrochemical approach is the possibility to acquire microscopic images during immersion and correlate those to OCP measurements. Figs. 5 and 6 show activity maps for each experimental condition at two kinetically significant points: the end of the induction period and the inflection point, with reference values given in Table 1. In these maps, the colour scale indicates activity level, with the brightest colours (orange/yellow) marking regions of highest activity. As mentioned before, highest activity corresponds to the high level of pixels changing over the surface. To support quantification, each original image was paired with a "mask" image that highlights the bright contrast. The fraction of the monitored area exhibiting high activity was calculated using ImageJ.

According to Fig. 5, at the end of the induction period, image analysis reveals notable differences among the tested acids and concentrations regarding the extent of high surface activity. Overall, the image background shows very low activity, which likely corresponds to the matrix phase. In contrast, high activity is observed in highly localised regions, likely due to preferential dissolution of the RE-rich phases and grain boundaries. For instance, NdFeB in 0.1 M formic acid already exhibited about 5 % of its monitored area with high activity level, but this is primarily associated with hydrogen bubble formation noticeable at the surface. As discussed before, these bubbles scatter light, causing temporary increases in the measured active area; however, detachment of the bubbles might show surface unchanged, depending on immersion period. In contrast, in 0.1 M citric acid the sample surface showed only 0.03 % of high active area; probably due to the short induction period (209 s). In the more diluted acids, the induction period is much longer (1378 s), and the fraction of highly active area remains low at this stage, 0.18–5 % from the analysed areas, confirming a localised and slower onset of dissolution.

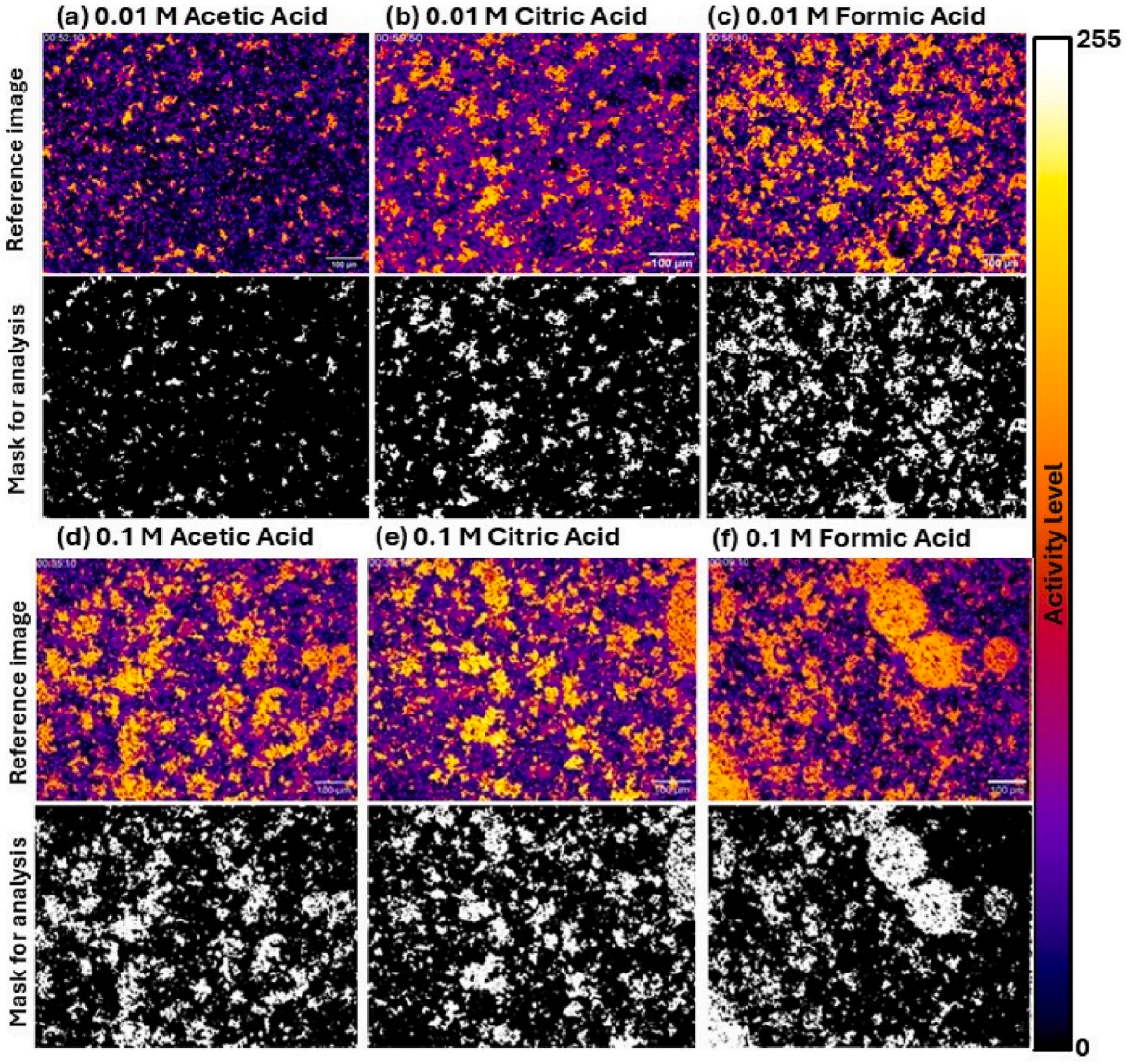

Fig. 6. Local activity maps of the NdFeB surface at the inflection point for each condition, with their corresponding mask images used for quantification of high-activity regions (red/orange contrast): (a) 0.01 M acetic acid, (b) 0.01 M citric acid, (c) 0.01 M formic acid, (d) 0.1 M acetic acid, (e) 0.1 M citric acid, and (f) 0.1 M formic acid.

When the inflection point is reached, with reference values shown in Table 1, the extent of high activity increases in most conditions, as seen in Fig. 6. All samples, except the one immersed in 0.01 M acetic acid, showed a substantial rise in active sites (orange-yellow contrast in terms of area fraction), 14–24 % from the analysed area, indicating the onset of rapid matrix activation that quickly propagates across a significant fraction of the monitored surface, particularly in concentrated solutions. However, for 0.01 M acetic acid, only 5 % of the analysed area displayed active sites and the background also showed minimal activity increase. This is unexpected given that, among the diluted solutions, this condition exhibited the shortest induction time and earliest inflection point. This apparent discrepancy may arise because the kinetic parameters are extracted from the mean activity level curves, which represent an average response across the entire monitored area. In contrast, the

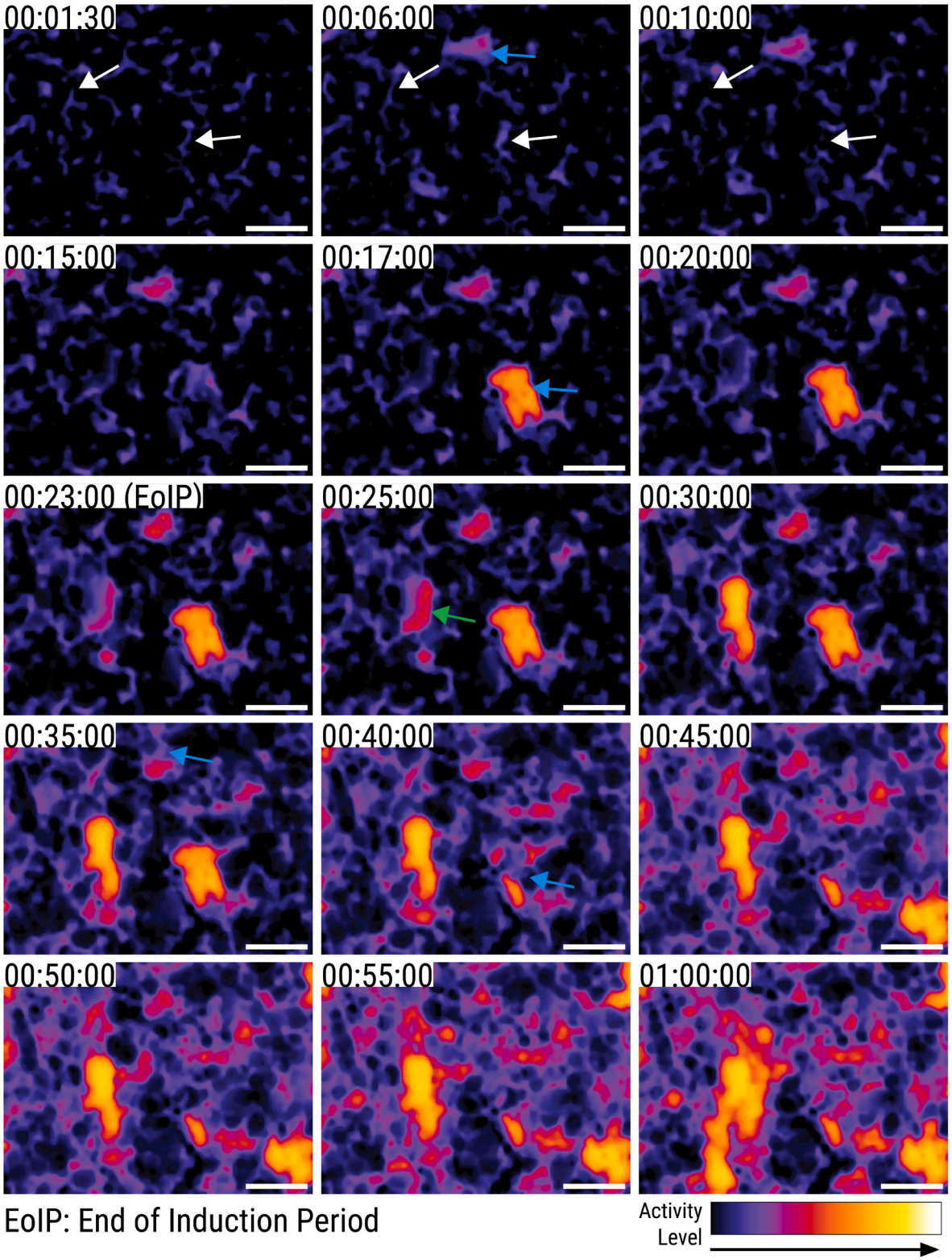

Fig. 7. Sequence of activity maps capturing surface changes in NdFeB in 0.01 M citric acid. Scale bar indicates 20 μm.

quantification of highly active sites is based on localised analysis, specifically targeting regions where the most significant pixel changes (orange-yellow contrast) are observed. As a result, the overall mean activity may suggest faster kinetics, while the spatial distribution of the most intense activity remains limited. This emphasises the high added-value of *in-situ* optical measurements.

Again, it is important to note that in 0.1 M formic acid, the rapid generation and detachment of hydrogen bubbles influenced the measured active area. Visual inspection of the images at the induction period confirms that most high-activity spots in these cases are attributable to bubbles. This experimental artifact necessitates cautious interpretation of the quantitative area fractions under such conditions.

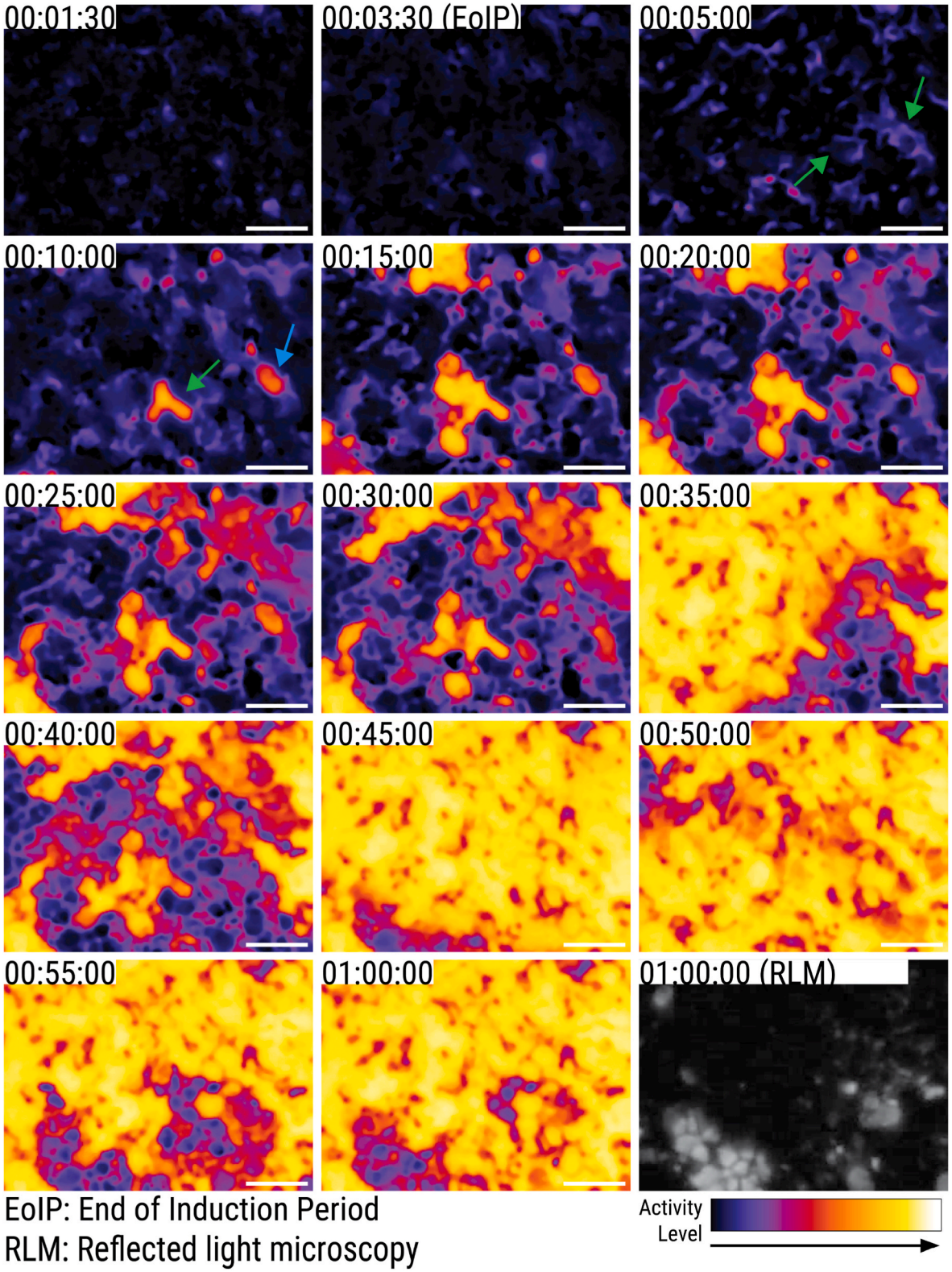

Fig. 8. Sequence of images capturing surface changes in NdFeB in 0.1 M citric acid. Scale bar indicates 20 μm.

The combination of electrochemical measurements with time-resolved image analysis provides a comprehensive perspective on the surface reactivity. The results underscore that both acid type and concentration significantly influence the onset, propagation, and overall extent of dissolution, but also highlight the importance of recognising and accounting for artifacts introduced by aggressive acidic conditions. When dissolution kinetic and OCP analyses are considered together, the imaging data reinforce a consistent mechanistic picture: more aggressive and concentrated acids accelerate and intensify surface activation, yet also introduce complexities, such as bubble formation, that must be carefully considered for reliable interpretation.

3.2.3.1. Time-images correlation of NdFeB in citric acid. To further explore the surface changes in NdFeB immersed in organic acids, Figs. 7 and 8 present selected time-lapse images showing local surface activity for samples immersed in 0.01 M and 0.1 M citric acid, respectively. Citric acid was chosen for its representative behaviour: at low concentration, it is similar to acetic and formic acids, and at higher concentration, its activity is intermediate between the two. For this analysis, a randomly selected area from the whole surface exposed and monitored was selected for better visualisation of the changes at the surface over the immersion time. Furthermore, enlarged images at specific times are also provided, highlighting significant changes in the surface activity. The area chose for 0.01 M citric acid is similar to the one shown in Fig. 3 (c) and 3 (d).

In 0.01 M citric acid, Fig. 7, active regions in the NdFeB sample, initially visible as narrow thread-like features with bluish contrast, appear as early as 1.5 min after immersion and connect gradually over time. These features are consistent with grain boundary darkening (Fig. 3 (c)) and is in agreement with initial dissolution of grain boundaries reported in literature [32]. Interestingly, this grain boundary activity can be initially reversible (see white arrows in Figs. 7–1.5 min–10 min) which suggests potential gas involvement, likely H_2 evolution. By 6 min, a large active site (indicated by the cyan arrow in Figs. 7–6 min), around 16 μm wide, is evident, possibly involving multiple grains, since the average grain size of the initial microstructure was 5.6 μm. This active site persisted but showed a drop-in activity on its top section at around 35 min (see cyan arrow in Figs. 7–35 min). This makes it an example of reversible grain darkening. The same behaviour is observed for the large active site which appeared at around 17 min (see cyan arrow in Figs. 7–17 min) and disappeared at around 40 min (see cyan arrow in Figs. 7–40 min). As with the reversible boundary darkening, this reversible grain domain darkening is potentially due to local hydrogen accumulation and its subsequent release. The high activity site which was first observed at around 25 min (see green arrow in Figs. 7–25 min). exhibited activity that gradually developed but persisted until the end of immersion. This makes it a potential candidate for irreversible grain domain darkening which could be attributed to the dissolution of the NdFeB matrix.

Consistent with Figs. 5 and 6, the activity maps in Fig. 7 show more frequent high-activity regions within the grain domains and an overall increase in matrix activity after the calculated induction period (1378 s), determined from the sigmoidal fit of the mean activity level curve (Table 1). Secondly, this supports the earlier hypothesis that surface changes do occur during the induction period, but the associated activity levels may remain low when averaged over the entire surface. Moreover, the increased matrix involvement after the induction period suggests that matrix dissolution becomes more substantial during the phase of rapid activity increase. It is important to note though that this dissolution is also potentially accompanied by increased frequency of gas accumulation.

Meanwhile in 0.1 M citric acid, Fig. 8, few spots exhibited higher activity than the matrix but there also appears to be some degree of changes on the matrix. Thread-like features similar to Fig. 7 (6 min) also became apparent at around 5 min, after the induction period. The thread-like features are accompanied by more visible changes (see green arrow in Figs. 8–5 min) on the matrix compared to the 0.01 M citric acid system. The increased matrix involvement is consistent with the higher activation observed after the induction period previously highlighted in Figs. 5 and 6. High-activity sites were detected at 10 min, much earlier than in dilute condition. One of the sites (see green arrow in Figs. 8–10 min) exhibited activity that persisted until the end of immersion, which suggests it is an example of irreversible grain darkening. Another site (see cyan arrow in Figs. 8–10 min) showed high activity that eventually faded at around 30 min which makes it an example of reversible grain darkening. After 30 min, most of the analysed area shows high activity, mainly due to formation of large hydrogen bubbles, as revealed by the changing contrast in images from 35 min to 45 min.

While distinguishing between the matrix and RE-rich phases based on these optical images is challenging, the earliest high-activity regions within thread-like structures possibly correspond to RE-rich phases (including the grain boundaries), with ongoing dissolution towards the matrix, as well as internally, i.e., perpendicular to the sample surface. A similar mechanism, consisting of initial localised activation followed by the expansion and interconnection of active sites, was also observed in acetic and formic acid, with higher activity typically concentrated at the center of each active site. Time-lapse videos for all conditions evaluated are provided in SI 3.

Relating these imaging findings to electrochemical data, steady-state OCP is generally considered indicative of matrix dissolution in NdFeB [63]. In Fig. 4, OCP stabilisation occurs within 300 s for most conditions, suggesting early onset of matrix attack, consistent with previous work [63]. However, the imaging data indicate that the matrix becomes notably more active around 1800 s for most conditions, except in 0.01 M formic acid. This difference highlights that OCP may reach steady-state while substantial surface transformation continues, likely due to the relatively large-exposed area and gradual progression of the dissolution process.

Local analyses indicate that matrix degradation can begin at early stages, even under dilute citric acid conditions. Intragranular activity was clearly observed during *in-situ* monitoring, suggesting that matrix dissolution does not occur exclusively at advanced immersion times. Khoshima et al. [36], however, reported selective leaching of REEs while preserving the $Nd_2Fe_{14}B$ matrix after 15 min of immersion in 0.1 M citric acid. This apparent discrepancy may arise from methodological differences: their conclusions were based on changes in the solid residue composition, whereas our time-resolved optical approach provides direct evidence of surface-level changes during the initial stages of dissolution. These findings underscore the value of localised, *in-situ* techniques in complementing bulk post-mortem analyses.

Thus, while activation observed in these images is a strong indicator of dissolution, only post analysis can definitively assess the extent and dissolution. For this reason, additional characterisation of the samples was performed after the experiments.

3.3. SEM-EDS characterisation after immersion

Fig. 9 shows the SEM images (BSE mode) of all samples after 1 h of immersion in different organic acids, except for the sample in 0.1 M formic acid, which had an immersion time of around 30 min. Additional images acquired in the SE mode at higher magnification, and EDS analyses can be found in SI 4. The areas analysed were randomly selected from the entire immersed surface and may not correspond to the specific region monitored by the microscopic camera.

Comparison of Fig. 9 with the initial microstructure shown in the inset (and in Fig. 2) demonstrates the significant impact of organic acid exposure on the NdFeB microstructure. In all cases, the RE-rich phases and grain boundaries are no longer visible, confirming their preferential dissolution, which is notably intensified at higher acid concentrations. This observation agrees with the earlier dissolution kinetic analysis, and it supports the interpretation that the earliest active sites detected

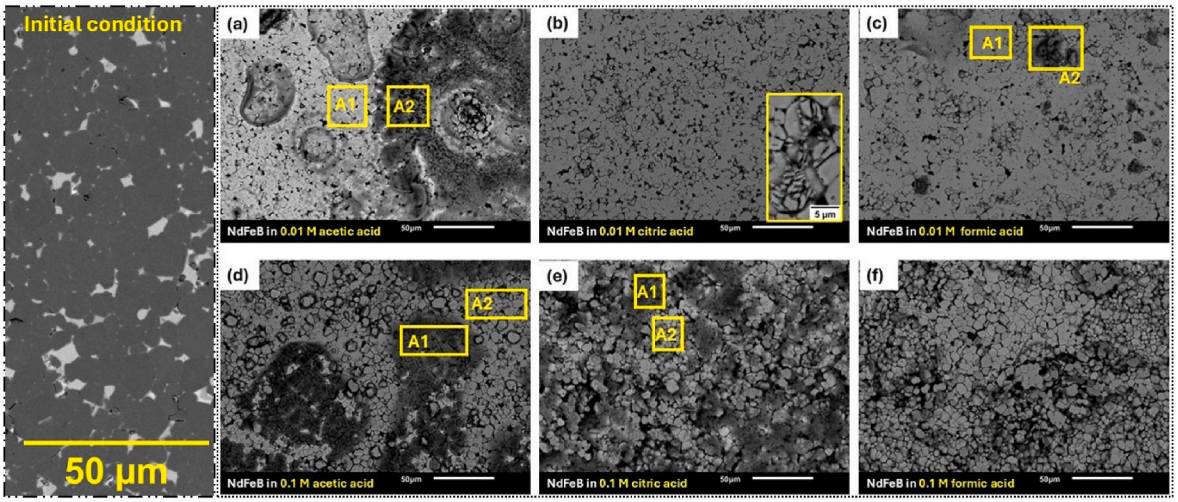

Fig. 9. Scanning backscattered electron images showing an example of the initial NdFeB microstructure as a reference for comparison with the surface morphologies after immersion in: (a) 0.01 M acetic acid for 1 h; (b) 0.01 M citric acid for 1 h (with an inset image to point out grain dissolution); (c) 0.01 M formic acid for 1 h; (d) 0.1 M acetic acid for 1 h; (e) 0.1 M citric acid for 1 h; (f) 0.1 M formic acid for 30 min.

optically, particularly those larger than grain boundaries (Figs. 6 and 7 at $t = 30$ s) reflect more extensive phase dissolution.

Regarding the dissolution of the NdFeB matrix itself, it was greatly influenced by both the nature and the concentration of the acid, but in all conditions the matrix was not fully dissolved. In 0.01 M acetic acid (Fig. 9(a)), besides the dissolution of the most actives phases, a crater (pit-like) morphology was found with dissolution products forming and depositing around these regions, e.g. A2 in Fig. 9 (a). This is confirmed by the high oxygen content measured by EDS (SI). The morphology seen in Fig. 9 (a) is similar to the "open pits" reported by Mao et al. [29]. At higher concentration of acetic acid (Fig. 9(d)), preferential oxidation areas (A1), with high oxygen content, and a significant grain boundary attack were observed.

For citric acid Fig. 9 (b) and (e), both RE-rich phase and grain boundary dissolution occurred, with more pronounced oxygen-rich regions and matrix attack at 0.1 M. The inset in Fig. 9 (b) highlights that matrix disintegration can occur within individual grains (intragranular dissolution), a phenomenon also seen for 0.1 M formic acid (see SI 4, Figure S7).

In 0.01 M formic acid, Fig. 9 (c), grain boundary dissolution was less evident than in other conditions. Localised regions of dark contrast (site A2) corresponded to areas with the lowest Fe content. This cannot be attributed to preferential Fe dissolution but rather the formation of insoluble complexes [19]. In the more aggressive 0.1 M formic acid, Fig. 9(f), although the sample was immersed for only 30 min, complete dissolution of the RE-rich phases was evident.

Overall, this study demonstrates that the complex dissolution mechanism of NdFeB magnets in organic acids is significantly influenced by both the nature and concentration of the chosen acid. The lack of a straightforward correlation between OCP and observed surface changes emphasises the dominant role of reaction kinetics in the dissolution process.

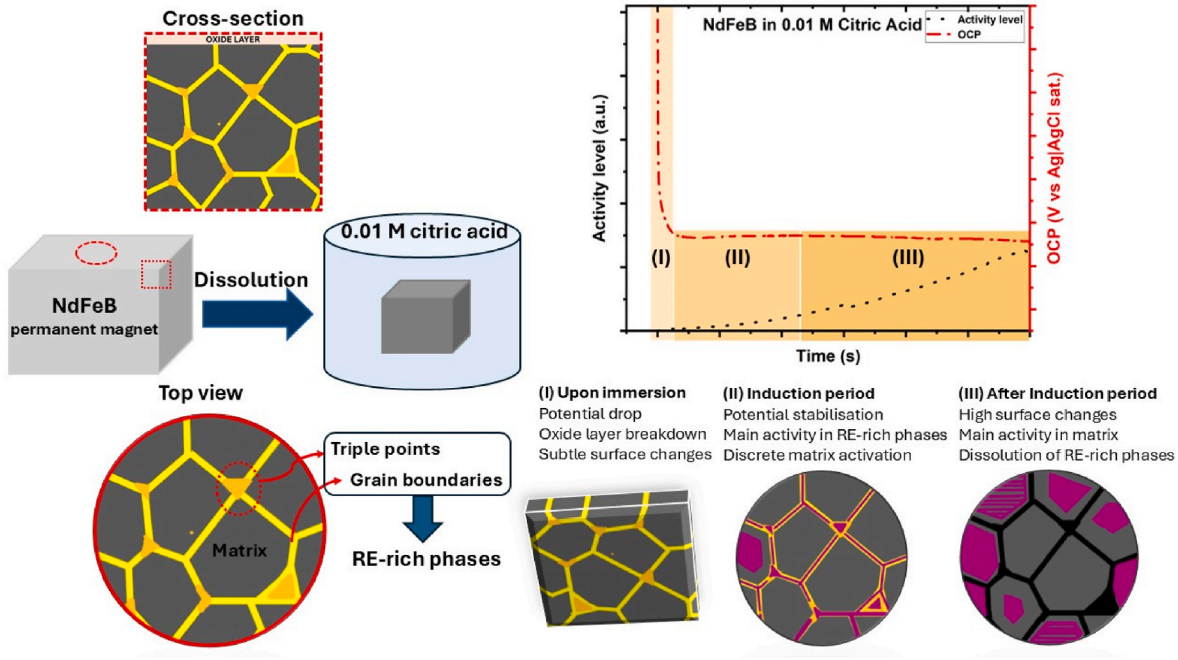

Fig. 10. Schematic representation of the proposed dissolution mechanism of NdFeB in 0.01 M citric acid, highlighting key stages observed during in situ monitoring.

The *in-situ* correlation between surface activity and dissolution behaviour highlighted the potential for controlled preferential dissolution of RE-rich phases at grain boundaries and triple points. Among the conditions tested, dilute citric acid (0.01 M) is particularly promising when operating within its induction period ~1378 s (23 min), as this condition balances an adequately time before rapid activation of the surface, which allows the monitoring of activity with intermediate reactivity compared to acetic and formic acids. An illustrative representation of NdFeB in diluted citric acid is shown in Fig. 10. In comparison with other selective-leaching routes, the measurements were carried out at room temperature and without externally applied potential or current; parameters known to influence dissolution kinetics. Operating under this low-energy, bias-free regime facilitates selectivity control and process simplicity, in contrast to routes requiring thermal pre-treatment (e.g., roasting prior to leaching), which entail substantially higher energy input [20].

Evidence of intragranular dissolution, also observed in 0.01 M citric acid (Fig. 9 (b)), suggests potential for preferential dissolution within the matrix phase. However, achieving practical selectivity within the matrix remains challenging due to minimal electrochemical differentiation between the matrix and RE-rich phases at the spatial resolution used in this study. Therefore, a more fundamental evaluation at a finer scale is recommended to further elucidate the mechanisms and enhance control over preferential dissolution. Nevertheless, for practical operational purposes, focusing dissolution efforts on grain boundaries and triple points with dilute citric acid currently represents the most viable strategy.

In perspective, this preferential dissolution can facilitate subsequent separation and purification steps, ultimately supporting more efficient and sustainable recovery of REEs from end-of-life NdFeB magnets. Nevertheless, quantitative yield and purity metrics would require, as next step, time-resolved leachate analysis (e.g., electrochemical cell coupled to ICP-OES/MS) and a detailed, process-level assessment of yield, purity, and sustainability via life-cycle assessment (LCA).

4. Conclusion

The dissolution of spent NdFeB permanent magnets was evaluated in acetic, citric and formic acids at concentrations of 0.01 M and 0.1 M at room temperature. For the first time, an optical-electrochemical set-up enabled the *in-situ* monitoring of surface changes while simultaneously measuring the open-circuit potential. This approach provided valuable insights into the preferential dissolution of REEs, which has traditionally been assessed only through *ex-situ* correlations. The key findings are summarised as follows.

- Since OCP did not vary significantly among the conditions, it was found that dissolution kinetics, rather than thermodynamic driving force, predominantly control the early-stage dissolution of NdFeB under the tested conditions.
- Quantitative analysis of activity level curves using sigmoidal fitting provided kinetic parameters, such as induction period, inflection point, and rate of change, which allowed for precise evaluation of the surface transformation under each condition.
- Higher acid concentrations led to much shorter induction periods (as low as 20 s) and earlier inflection points (as early as 542 s), while lower concentrations resulted in longer induction periods (up to 1500 s) and delayed, more gradual transitions, which demonstrates the strong effect of acid concentration on dissolution rate.
- *In-situ* analysis enabled to characterise the overall mechanism: an initial localised activation, followed by the formation of thread-like structures and the subsequent expansion and interconnection of active sites.
- 0.01 M citric acid was pointed out as potential medium for controlled RE-rich dissolution within its induction period (~23 min). Intragranular dissolution was also observed in this condition, highlighting the possibility, of controlled extracting REEs from within the grains.

Declaration of competing interest

The authors declare that they have no known competing financial interests or personal relationships that could have appeared to influence the work reported in this paper.

Acknowledgments

This work is a part of the REEcycle project, funded by the European Union under the HORIZON 2020 - Marie Sklodowska Curie Actions Postdoctoral Fellowship granted to Camila Pucci Couto, project number: 101106819. Additionally, the authors thank the company SUEZ for providing end-of-life products with NdFeB permanent magnets. JU acknowledges financial support to the Fédération Wallonie-Bruxelles for the ARC-Consolidator grant RENEGADE. MM acknowledges the financial support from DOST ERDT Program.

Appendix A. Supplementary data

Supplementary data to this article can be found online at https://doi.org/10.1016/j.jmrt.2025.11.006.

Data availability

The raw/processed data required to reproduce these findings can be shared by contacting the corresponding author.

References

[1] Nations U. United nations climate change 2023 highlights. https://unfccc.int/about-us/2023-highlights; 2023.
[2] European Commission. EU at COP28 climate change conference. https://commission.europa.eu/strategy-and-policy/priorities-2019-2024/european-green-deal/climate-action-and-green-deal/eu-un-climate-change-conference/eu-cop28-climate-change-conference_en; 2023.
[3] Couto CP, van de Ven JJMM, Yang Y, Abrahami ST. On the pre-treatment for recycling spent NdFeB permanent magnets: from disassembling, characterisation to de-coating. Sustain Mater Technol 2024;41:e01041. https://doi.org/10.1016/j.susmat.2024.e01041.
[4] Balaram V. Rare earth elements: a review of applications, occurrence, exploration, analysis, recycling, and environmental impact. Geosci Front 2019;10:1285–303. https://doi.org/10.1016/j.gsf.2018.12.005.
[5] Binnemans K, Jones PT, Blanpain B, Van Gerven T, Yang Y, Walton A, et al. Recycling of rare earths: a critical review. J Clean Prod 2013;51:1–22. https://doi.org/10.1016/j.jclepro.2012.12.037.
[6] Kumari A, Kumar Sahu S. A comprehensive review on recycling of critical raw materials from spent neodymium iron boron (NdFeB) magnet. Sep Purif Technol 2023;317:123527. https://doi.org/10.1016/j.seppur.2023.123527.
[7] Abrahami ST, Xiao Y, Yang Y. Rare-earth elements recovery from post-consumer hard-disc drives. Trans Institutions Min Metall Sect C Miner Process Extr Metall 2015;124:106–15. https://doi.org/10.1179/1743285514Y.0000000084.
[8] Yang Y, Walton A, Sheridan R, Güth K, Gauß R, Gutfleisch O, et al. REE recovery from end-of-life NdFeB permanent magnet scrap: a critical review. J Sustain Metall 2017;3:122–49. https://doi.org/10.1007/s40831-016-0090-4.
[9] Omodara L, Pitkäaho S, Turpeinen EM, Saavalainen P, Oravisjärvi K, Keiski RL. Recycling and substitution of light rare earth elements, cerium, lanthanum, neodymium, and praseodymium from end-of-life applications - a review. J Clean Prod 2019;236. https://doi.org/10.1016/j.jclepro.2019.07.048.
[10] European Commission. Study on the critical raw materials for the EU. https://doi.org/10.2873/725585; 2023.
[11] Liu Q, Sun K, Ouyang X, Sen B, Liu L, Dai T, et al. Tracking three decades of global neodymium stocks and flows with a trade-linked multiregional material flow analysis. Environ Sci Technol 2022;56:11807–17. https://doi.org/10.1021/acs.est.2c02247.
[12] European Commission. Press release Critical Raw Materials: ensuring secure and sustainable supply chains for EU's green and digital future. 2023.
[13] European Commission. EU secures access to diversified, affordable, and sustainable supply of critical raw materials. https://luxembourg.representation.ec.europa.eu/actualites-et-evenements/actualites/eu-secures-access-diversified-affordable-and-sustainable-supply-critical-raw-materials-2024-05-23_en?prefLang=pt. [Accessed 1 October 2024].

[14] Venkatesan P, Vander Hoogerstraete T, Hennebel T, Binnemans K, Sietsma J, Yang Y. Selective electrochemical extraction of REEs from NdFeB magnet waste at room temperature. Green Chem 2018;20:1065–73. https://doi.org/10.1039/C7GC03296J.
[15] Venkatesan P, Sun ZHI, Sietsma J, Yang Y. An environmentally friendly electro-oxidative approach to recover valuable elements from NdFeB magnet waste. Sep Purif Technol 2018;191:384–91. https://doi.org/10.1016/j.seppur.2017.09.053.
[16] Venkatesan P, Vander Hoogerstraete T, Binnemans K, Sun Z, Sietsma J, Yang Y. Selective extraction of rare-earth elements from NdFeB magnets by a room-temperature electrolysis pretreatment step. ACS Sustainable Chem Eng 2018;6:9375–82. https://doi.org/10.1021/acssuschemeng.8b01707.
[17] Kumari A, Dipali Randhawa NS, Sahu SK. Electrochemical treatment of spent NdFeB magnet in organic acid for recovery of rare earths and other metal values. J Clean Prod 2021;309:127393. https://doi.org/10.1016/j.jclepro.2021.127393.
[18] Kumari A, Kumar M, Pramanik S, Kumar S. Recovery of rare earths from spent NdFeB magnets of wind turbine : leaching and kinetic aspects. Waste Manag 2020;75:486–98. https://doi.org/10.1016/j.wasman.2018.01.033.
[19] Belfqueh S, Seron A, Chapron S, Arrachart G, Menad N. Evaluating organic acids as alternative leaching reagents for rare earth elements recovery from NdFeB magnets. J Rare Earths 2023;41:621–31. https://doi.org/10.1016/j.jre.2022.04.027.
[20] Gergoric M, Ravaux C, Steenari BM, Espegren F, Retegan T. Leaching and recovery of rare-earth elements from neodymium magnet waste using organic acids. Metals 2018;8:1–17. https://doi.org/10.3390/met8090721.
[21] Choubey PK, Singh N, Panda R, Jyothi RK, Yoo K, Park I, et al. Development of hydrometallurgical process for recovery of rare Earth metals (Nd, Pr, and dy) from Nd-Fe-B magnets. Metals 2021;11:1987. https://doi.org/10.3390/met11121987.
[22] Tunsu C. Hydrometallurgy in the recycling of spent NdFeB permanent magnets. Elsevier Ltd; 2018. https://doi.org/10.1016/B978-0-08-102057-9.00008-1.
[23] Zhang Y, Gu F, Su Z, Liu S, Anderson C, Jiang T. Hydrometallurgical recovery of rare earth elements from ndfeb permanent magnet scrap: a review. Metals 2020;10:1–34. https://doi.org/10.3390/met10060841.
[24] Coelho F, Abrahami S, Yang Y, Sprecher B, Li Z, Menad N-E, et al. Upscaling of permanent magnet dismantling and recycling through VALOMAG Project. Int. Conf. Raw mater. Circ. Econ. Basel Switzerland: MDPI; 2021. p. 74. https://doi.org/10.3390/materproc2021005074.
[25] Vander Hoogerstraete T, Blanpain B, Van Gerven T, Binnemans K. From NdFeB magnets towards the rare-earth oxides: a recycling process consuming only oxalic acid. RSC Adv 2014;4:64099–111. https://doi.org/10.1039/c4ra13787f.
[26] Önal MAR, Borra CR, Guo M, Blanpain B, Van Gerven T. Recycling of NdFeB magnets using sulfation, selective roasting, and water leaching. J Sustain Metall 2015;1:199–215. https://doi.org/10.1007/s40831-015-0021-9.
[27] Laatikainen M, Makarova I, Sainio T, Repo E. Selective acid leaching of rare earth elements from roasted NdFeB magnets. Sep Purif Technol 2022;278:119571. https://doi.org/10.1016/j.seppur.2021.119571.
[28] Makarova I, Soboleva E, Osipenko M, Kurilo I, Laatikainen M, Repo E. Electrochemical leaching of rare-earth elements from spent NdFeB magnets. Hydrometallurgy 2020;192:105264. https://doi.org/10.1016/j.hydromet.2020.105264.
[29] Mao S, Yang H, Song Z, Li J, Ying H, Sun K. Corrosion behaviour of sintered NdFeB deposited with an aluminium coating. Corros Sci 2011;53:1887–94. https://doi.org/10.1016/j.corsci.2011.02.006.
[30] El-Moneim AA, Gebert A. Electrochemical characterization of galvanically coupled single phases and nanocrystalline NdFeB-based magnets in NaCl solutions. J Appl Electrochem 2003;33:795–805. https://doi.org/10.1023/A:1025548411091.
[31] Bala H, Szymura S, Pawłowska G, Rabinovich YM. Effect of impurities on the corrosion behaviour of neodymium. J Appl Electrochem 1993;23:1017–24. https://doi.org/10.1007/BF00266123.
[32] Schultz L, El-Aziz AM, Barkleit G, Mummert K. Corrosion behaviour of Nd-Fe-B permanent magnetic alloys. Mater Sci Eng, A 1999;267:307–13. https://doi.org/10.1016/S0921-5093(99)00107-0.
[33] Song YW, Zhang H, Yang HX, Song ZL. A comparative study on the corrosion behavior of NdFeB magnets in different electrolyte solutions. Mater Corros 2008;59:794–801. https://doi.org/10.1002/maco.200804175.
[34] Zakotnik M, Harris IR, Williams AJ. Possible methods of recycling NdFeB-type sintered magnets using the HD/degassing process. J Alloys Compd 2008;450:525–31. https://doi.org/10.1016/j.jallcom.2007.01.134.
[35] Degri MJJ. The processing and characterisation of recycled NdFeB-type sintered magnets. School of Metallurgy and Materials, University of Birmingham; 2014. PhD thesis, Available on: https://etheses.bham.ac.uk/id/eprint/5516/1/Degri14PhD.pdf.
[36] Khoshsima S, Vidmar J, Samardžija Z, Tomše T, Kušter M, Mishra A, et al. Environmentally friendly approach for Nd2Fe14B magnetic phase extraction by selective chemical leaching: a proof-of-concept study. Materials 2023;16. https://doi.org/10.3390/ma16145181.
[37] Mishra A, Khoshsima S, Tomše T, Podmiljšak B, Šturm S, Burkhardt C, et al. Short-loop recycling of Nd-Fe-B permanent magnets: a sustainable solution for the RE2Fe14B matrix phase recovery. Materials 2023;16:1–13. https://doi.org/10.3390/ma16196565.
[38] Gurrappa I, Pandian S. Corrosion characteristics of Nd-Fe-B permanent magnets in different environments. Corrosion Eng Sci Technol 2006;41:57–61. https://doi.org/10.1179/174327806X94018.
[39] Gurappa I. Corrosion characteristics of permanent magnets in acidic environments. J Alloys Compd 2003;360:236–42. https://doi.org/10.1016/S0925-8388(03)00359-1.
[40] Sueptitz R, Uhlemann M, Gebert A, Schultz L. Corrosion, passivation and breakdown of passivity of neodymium. Corros Sci 2010;52:886–91. https://doi.org/10.1016/j.corsci.2009.11.008.
[41] Zheng J, Jiang L, Chen Q. Electrochemical corrosion behavior of Nd-Fe-B sintered magnets in different acid solutions. J Rare Earths 2006;24:218–22. https://doi.org/10.1016/S1002-0721(06)60097-5.
[42] Barkleit G, Ei-Aziz AM, Schneider F, Mummert K. Characterisation of electrochemical interactions between single phases of Nd-Fe-B permanent magnets. Werkst Korros 2001;52:193–200. https://doi.org/10.1002/1521-4176(200103)52:3<193::aid-maco193>3.0.co;2-s.
[43] Denissen PJ, Garcia SJ. Cerium-loaded algae exoskeletons for active corrosion protection of coated AA2024-T3. Corros Sci 2017;128:164–75. https://doi.org/10.1016/j.corsci.2017.09.019.
[44] Denissen PJ, Garcia SJ. Reducing subjectivity in EIS interpretation of corrosion and corrosion inhibition processes by in-situ optical analysis. Electrochim Acta 2019;293:514–24. https://doi.org/10.1016/j.electacta.2018.10.018.
[45] Denissen PJ, Homborg AM, Garcia SJ. Interpreting electrochemical noise and monitoring local corrosion by means of highly resolved spatiotemporal real-time optics. J Electrochem Soc 2019;166:C3275–83. https://doi.org/10.1149/2.0341911jes.
[46] Olgiati M, Denissen PJ, Garcia SJ. When all intermetallics dealloy in AA2024-T3: quantifying early stage intermetallic corrosion kinetics under immersion. Corros Sci 2021;192. https://doi.org/10.1016/j.corsci.2021.109836.
[47] Mopon M, Mol A, Garcia SJ. Effect of delayed inhibitor supply on AA2024-T3 intermetallic activity: a local in situ analysis with reflected microscopy. Corros Sci 2024;230:111910. https://doi.org/10.1016/j.corsci.2024.111910.
[48] Mopon M, Mol A, Garcia SJ. Intermetallic particles trigger streaking corrosion in AA7075-T6. npj Mater Degrad9 2025;92. https://doi.org/10.1038/s41529-025-00631-5.
[49] Mopon M, Sc M, Mol A, Garcia SJ. Local re-immersion behaviour of Ce-based inhibiting layers on AA2024-T3 intermetallics: enhanced stability through partial dealloying and prolonged exposure (accepted). Corros Sci 2025;255:113146. https://doi.org/10.1016/j.corsci.2025.113146.
[50] Makogon A, Bertolucci Coelho L, Ustarroz J, Decorse P, Kanoufi F, Shkirskiy S. Machine learning-enhanced optical monitoring for identifying pitting-susceptible zones in 316L stainless steel. Corros Sci 2025;256:113184. https://doi.org/10.1016/j.corsci.2025.113184.
[51] Makogon A, Noël JM, Kanoufi F, Shkirskiy V. Deciphering the interplay between local and global dynamics of anodic metal oxidation. Anal Chem 2024;96:1129–37. https://doi.org/10.1021/acs.analchem.3c04160.
[52] Godeffroy L, Makogon A, Gam Derouich S, Kanoufi F, Shkirskiy V. Imaging and quantifying the chemical communication between single particles in metal alloys. Anal Chem 2023;95:9999–10007. https://doi.org/10.1021/acs.analchem.3c01258.
[53] Behera SS, Parhi PK. Leaching kinetics study of neodymium from the scrap magnet using acetic acid. Sep Purif Technol 2016;160:59–66. https://doi.org/10.1016/j.seppur.2016.01.014.
[54] Behera SS, Panda SK, Mandal D, Parhi PK. Ultrasound and microwave assisted leaching of neodymium from waste magnet using organic solvent. Hydrometallurgy 2019;185:61–70. https://doi.org/10.1016/j.hydromet.2019.02.003.
[55] ASTM. Standard Test methods for determining average grain sizeE112. ASTM; 2024.
[56] Sepehri-Amin H, Ohkubo T, Shima T, Hono K. Grain boundary and interface chemistry of an Nd-Fe-B-based sintered magnet. Acta Mater 2012;60:819–30. https://doi.org/10.1016/j.actamat.2011.10.043.
[57] Murakami Y, Tanigaki T, Sasaki TT, Takeno Y, Park HS, Matsuda T, et al. Magnetism of ultrathin intergranular boundary regions in Nd-Fe-B permanent magnets. Acta Mater 2014;71:370–9. https://doi.org/10.1016/j.actamat.2014.03.013.
[58] Sasaki TT, Ohkubo T, Hono K. Structure and chemical compositions of the grain boundary phase in Nd-Fe-B sintered magnets. Acta Mater 2016;115:269–77. https://doi.org/10.1016/j.actamat.2016.05.035.
[59] Gaona-Tiburcio C, Almeraya-Calderón F, Chacon-Nava JG, Matutes-Aquino JA, Martinez-Villafañe A. Electrochemical response of permanent magnets in different solutions. J Alloys Compd 2004;369:78–80. https://doi.org/10.1016/j.jallcom.2003.09.050.
[60] dos Santos CAL, Panossian Z. Permanent rare-earth Magnets—The need to protect them against corrosion. Mater Sci Appl 2019;10:317–27. https://doi.org/10.4236/msa.2019.104024.
[61] Ahmad Z. Principles of corrosion engineering and corrosion control. Elsevier Ltd; 2004.
[62] Bentea L, Watzky MA, Finke RG. Sigmoidal nucleation and growth curves across Nature fit by the Finke-Watzky model of slow continuous nucleation and autocatalytic growth: explicit formulas for the lag and growth times plus other key insights. J Phys Chem C 2017;121:5302–12. https://doi.org/10.1021/acs.jpcc.6b12021.
[63] El-Moneim AA, Gebert A, Schneider F, Gutfleisch O, Schultz L. Grain growth effects on the corrosion behavior of nanocrystalline NdFeB magnets. Corros Sci 2002;44:1097–112. https://doi.org/10.1016/S0010-938X(01)00123-8.